

Time delay interferometry with minimal null frequencies

Gang Wang^{1,*}

¹*Shanghai Astronomical Observatory, Chinese Academy of Sciences, Shanghai 200030, China*
(Dated: March 5, 2024)

Time delay interferometry (TDI) is a key technique employed in gravitational wave (GW) space missions to mitigate laser frequency noise by combining multiple laser links and establishing an equivalent equal arm interferometry. The null frequencies will be introduced in noise spectra and GW response when the periodical signal/noise is canceled in synthesized laser links. These frequencies are characteristic frequencies (CFs) of a TDI which related to its geometry of combination. In this work, we propose a second-generation TDI configuration referred to as hybrid Relay, whose CFs are only one-quarter that of the fiducial second-generation Michelson observables. We examine the performance of novel TDI configuration in laser noise cancellation and clock noise suppression and justify its essential capabilities. To assess its robustness for signal extraction, we simulate data containing GW signals from massive black hole binaries and perform parameter inferences with comparisons against the fiducial Michelson TDI configuration. The results demonstrate that the newly proposed TDI solution could be more robust than Michelson in fulfilling data analysis.

I. INTRODUCTION

LISA is scheduled to be launched in the mid-2030s with a mission to observe gravitational waves (GWs) in the milli-Hz band [1, 2]. The detector comprises three spacecraft (S/C) forming a triangular constellation, utilizing laser interferometry between S/C to monitor the distance fluctuations caused by GWs. However, due to orbital dynamics and laser stability limitations, laser frequency noise may dominate GW signal in inter-S/C measurements.

To address this challenge and achieve the target sensitivity, time-delay interferometry (TDI) has been developed, synthesizing multiple laser links to form an equivalent equal-arm interferometer [3]. Various TDI configurations have been devised with different abilities to suppress laser noise. The first-generation TDI cancels laser noise in a static unequal arm constellation [3–11, and references therein], while the second-generation TDI further suppresses laser noise in time-varying arm lengths [12–18, and references therein]. Modified TDI formulations driven by data analysis have been developed to comprehensively resolve laser noise and/or signals [19–23]. Furthermore, advancements in inter-S/C measurement designs have enabled the reduction of clock noise in TDI [24–28].

Current TDI studies primarily focused on the Michelson configuration, which mimics the original Michelson and employs four laser links in two interferometric arms, synthesizing the measurements recurrently. However, the symmetric geometry introduces null frequencies or characteristic frequencies (CFs) where the periodic signals and noises are significantly canceled. Additionally, differences between unequal arms result in non-identical observables from different two arms. These properties of Michelson TDI could raise numerical challenges for data

analysis.

In this study, we propose an alternative TDI observables referred to as hybrid Relay. These observables have only one-quarter CFs of second-generation Michelson, resulting in smoother noise spectra and GW response functions. As a second-generation TDI configuration, the new observables could sufficiently suppress laser frequency noise and clock noise as the Michelson observables. Another advantage is that the optimal TDI channels from the new configuration would be more robust than Michelson, avoiding susceptibility to unequal arm lengths during orbital motion. To validate the performance of the proposed TDI configuration, simulation and analysis are conducted using SATDI [29]. With the data containing GW signals from massive binary black holes (MBBH), the hybrid Relay demonstrates a stable capability to yield reliable results, making it a promising TDI candidate for space missions GW data processing.

This paper is organized as follows: We introduce the hybrid Relay TDI configuration and its geometry in Section II. In Section III, the capabilities of laser noise suppression and clock noise cancellation are examined for proposed TDI observables, and the averaged sensitivities are evaluated for the ordinary and optimal channels. The data simulation and GW analysis are presented in Section IV. Post-analysis further reveals the disadvantages of the Michelson configuration and the advantages of the hybrid Relay. A brief conclusion and discussion are given in Section V. (We set $G = c = 1$ in this work except specified in the equations.)

II. TIME DELAY INTERFEROMETRY OF HYBRID RELAY

The first-generation TDI configurations were developed to mitigate laser noise caused by static unequal arm interferometry, as specified in references [3, 4, 30]. These configurations consist of five groups: Sagnac (α, β, γ), Michelson (X, Y, Z), Relay (U, V, W), Monitor (D, F,

* Gang Wang: gwang@shao.ac.cn, gwanggw@gmail.com

G), and Beacon (P, Q, R). Of particular relevance to this study are the Michelson and Relay, and their first observables are expressed as

$$\begin{aligned} X &= (\mathcal{D}_{31}\mathcal{D}_{13}\mathcal{D}_{21}\eta_{12} + \mathcal{D}_{31}\mathcal{D}_{13}\eta_{21} + \mathcal{D}_{31}\eta_{13} + \eta_{31}) \\ &\quad - (\eta_{21} + \mathcal{D}_{21}\eta_{12} + \mathcal{D}_{21}\mathcal{D}_{12}\eta_{31} + \mathcal{D}_{21}\mathcal{D}_{12}\mathcal{D}_{31}\eta_{13}), \\ U &= (\eta_{13} + \mathcal{D}_{13}\eta_{21} + \mathcal{D}_{21}\mathcal{D}_{13}\eta_{32} + \mathcal{D}_{32}\mathcal{D}_{21}\mathcal{D}_{13}\eta_{23}) \\ &\quad - (\eta_{23} + \mathcal{D}_{23}\eta_{32} + \mathcal{D}_{32}\mathcal{D}_{23}\eta_{13} + \mathcal{D}_{13}\mathcal{D}_{23}\mathcal{D}_{32}\eta_{21}), \end{aligned} \quad (1)$$

where \mathcal{D}_{ij} is a delay operator, $\mathcal{D}_{ij}y = y(t - L_{ij})$, η_{ij} is measurement combination in a laser link from S/C*i* to S/C*j* as specified in [29]. Three additional observables, (\bar{U} , \bar{V} , \bar{W}), could be derived by adjusting the path of Relay, and the first channel could be formulated as

$$\begin{aligned} \bar{U}(t) &= (\eta_{32} + \mathcal{D}_{32}\eta_{23} + \mathcal{D}_{32}\mathcal{D}_{23}\eta_{12} + \mathcal{D}_{32}\mathcal{D}_{23}\mathcal{D}_{12}\eta_{31}) \\ &\quad - (\eta_{12} + \mathcal{D}_{12}\eta_{31} + \mathcal{D}_{12}\mathcal{D}_{31}\eta_{23} + \mathcal{D}_{12}\mathcal{D}_{31}\mathcal{D}_{23}\eta_{32}). \end{aligned} \quad (2)$$

More lucid expressions of three TDI observables are illustrated through geometric diagrams in Fig. 1 [31, 32]. The vertical lines represent the trajectories of three S/C (\textcircled{i} ($i = 1, 2, 3$), and duplicated S/C2 and S/C3 are plotted in the Relay-U and $-\bar{U}$ diagrams to prevent intersections around non-integer delay ticks. The blue and magenta lines depict the combined links for the virtual interferometer of two beams. The δt represents the mismatches for the two beams due to the orbital dynamics.

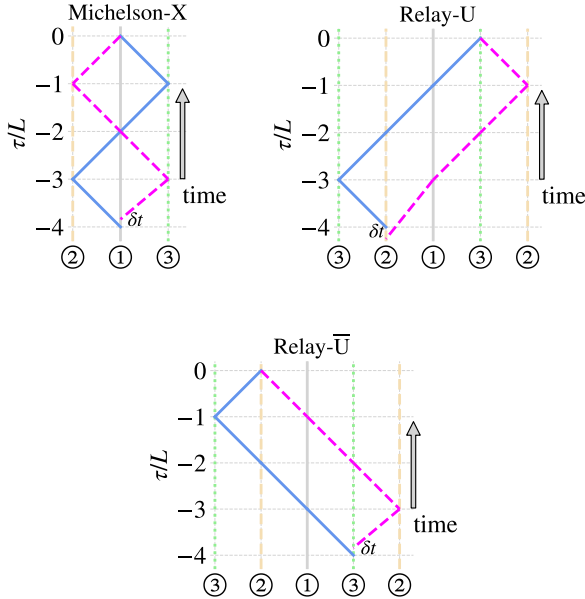


FIG. 1. The geometric diagrams for selected first-generation TDI channels. The vertical lines indicate the trajectories of three S/C (\textcircled{i} ($i = 1, 2, 3$), and the horizon is the separation between S/C. The blue and magenta lines depict two groups of combined laser links TDI.

Numerous second-generation TDI observables can be constructed from first-generation or other methods [18,

33, 34]. As the fiducial configuration, the second-generation TDI Michelson observables ($X1$, $Y1$, $Z1$) are derived by combining two of its first-generation TDI observables with a proper delay. For instance, $X1$ could be expressed as

$$X1(t) \simeq X(t - 4L) - X(t), \quad (3)$$

and its diagram is shown in the left plot of Fig. 2. The $Y1$ and $Z1$ could be obtained through cyclical permutation of links' indexes. Hybrid Relay observables could be generated by combining U and delayed \bar{U} , denoted as $U\bar{U}$, and vice versa. They can be expressed as

$$U\bar{U}(t) \simeq U(t) + \bar{U}(t - 4L), \quad (4)$$

$$\bar{U}U(t) \simeq \bar{U}(t) + U(t - 4L). \quad (5)$$

The diagram of $U\bar{U}$ is shown in the right plot of Fig. 2. These observables could further suppress the laser noise during S/C motion and should be categorized as a second-generation TDI. Triple observables originating from three different S/C will be denoted as ($U\bar{U}$, $V\bar{V}$, $W\bar{W}$) or ($\bar{U}U$, $\bar{V}V$, $\bar{W}W$). Considering the performances of these two sets are effectively identical, the former group is elected for comparison with the fiducial Michelson observables ($X1$, $Y1$, $Z1$).

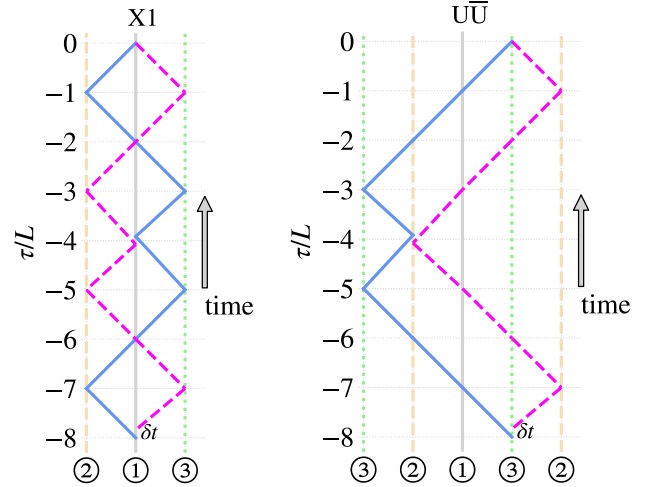


FIG. 2. The geometric diagrams for $X1$ and $U\bar{U}$.

From three ordinary TDI observables (a, b, c), three (quasi-)orthogonal or optimal observables, (A, E, T) can be constructed [35],

$$\begin{bmatrix} A \\ E \\ T \end{bmatrix} = \begin{bmatrix} -\frac{1}{\sqrt{2}} & 0 & \frac{1}{\sqrt{2}} \\ \frac{1}{\sqrt{6}} & -\frac{2}{\sqrt{6}} & \frac{1}{\sqrt{6}} \\ \frac{1}{\sqrt{3}} & \frac{1}{\sqrt{3}} & \frac{1}{\sqrt{3}} \end{bmatrix} \begin{bmatrix} a \\ b \\ c \end{bmatrix}. \quad (6)$$

The A and E are expected to the science channels which can respond to GW signals effectively, while the T channel will be a noise-dominated data stream used to characterize instrumental noises. To distinguish the optimal

channels from different TDI configurations, a subscript of the first ordinary TDI is added to A/E/T. For instance, A_{X1} indicates the A channel generated from (X1, Y1, Z1).

III. NOISE SUPPRESSIONS AND SENSITIVITY

A. Suppressions of laser noise and clock noise

The primary objective of TDI is to suppress the dominant laser noises. To assess the effectiveness of TDI observables, the lasers are assumed to have a stability of $30 \text{ Hz}/\sqrt{\text{Hz}}$ which corresponds to a noise power-spectral density (PSD) of $1 \times 10^{-26} \text{ /Hz}$. By employing a numerical orbit for LISA, the mismatches, δt , for X1 and $U\bar{U}$ are within the ranges of $[-10, 10]$ ps and $[-6, 6]$ ps, respectively [32, 36, 37]. These mismatches are sufficiently small to theoretically meet the requirement for laser noise suppression. However, another critical factor influencing laser noise cancellation is the ranging error between two S/C. The post-processing ranging time between S/C could have a noise with PSD of $10^{-15} \frac{\text{Hz}}{f} \text{ s}/\sqrt{\text{Hz}}$ and an additional bias of 3 ns (0.9 m) [38, 39]. With these noise assumptions, the residual laser noises in X1 and $U\bar{U}$ are evaluated and shown in the upper panel of Fig. 3. The secondary noises, including acceleration noise and optical metrology noise, are plotted in the plot for comparison. The noise budgets for acceleration noise S_{acc} and optical path noise S_{op} are as follows [1],

$$\begin{aligned} \sqrt{S_{\text{acc}}} &= 3 \frac{\text{fm}/\text{s}^2}{\sqrt{\text{Hz}}} \sqrt{1 + \left(\frac{0.4\text{mHz}}{f}\right)^2} \sqrt{1 + \left(\frac{f}{8\text{mHz}}\right)^4}, \\ \sqrt{S_{\text{op}}} &= 10 \frac{\text{pm}}{\sqrt{\text{Hz}}} \sqrt{1 + \left(\frac{2\text{mHz}}{f}\right)^4}. \end{aligned} \quad (7)$$

From the plot, it is evident that the residual laser noises in two TDI channels are orders of magnitude lower than the secondary noises, indicating that the TDI solutions are effective for laser noise suppressions.

After the laser noise is suppressed, the clock noise becomes the key noise affecting sensitivity. Following the method developed in [27], clock noise is assessed for both X1 and $U\bar{U}$ by assuming a clock noise of $4 \times 10^{-27}/f$ in fractional frequency deviations. The results, depicted in the lower panel of Fig. 3, demonstrate that the clock noise can be significantly reduced for both Michelson and hybrid Relay. Hence, the current approach to clock noise cancellation is applicable to the new TDI configuration.

From Fig. 3, we can notice that CFs of X1 for either laser noise, secondary noise, or (original) clock noise emerge at $n/(4L) \simeq 0.03n \text{ Hz}$, $n = 1, 2, 3, \dots$ and L is the arm length of constellation. In contrast, the CFs of $U\bar{U}$ only appear at the $n/L \simeq 0.12n \text{ Hz}$. With only one-fourth of CFs, the noise spectra of hybrid Relay are smoother and more stable than those of Michelson On

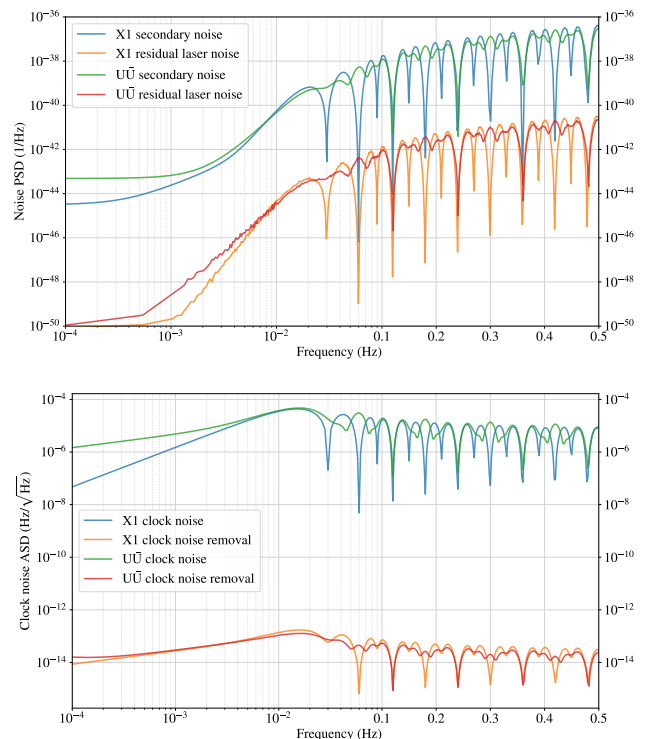


FIG. 3. The laser noise (upper) and clock noise (lower) suppressions in X1 and $U\bar{U}$ observables. (A log scale is used for frequencies lower than 0.1 Hz, and a linear scale is employed for frequencies higher than 0.1 Hz. This mixed x-axis scale is utilized in the following frequency-domain plots).

the other side, the frequencies $f_c = n/L$ imply that the integral circle of noise/signal in a single inter-S/C links representing the minimum common CFs that all TDI observables will possess. And hybrid Relay observables ($U\bar{U}$, $V\bar{V}$, $W\bar{W}$) only have these minimum CFs.

B. Average sensitivities

The average sensitivity over all sky directions indicates the detectability of a TDI observable. The sensitivities of $U\bar{U}$ and the corresponding optimal channels are evaluated by using the algorithm in [32], and the results are shown in Fig. 4. The PSDs of secondary noises are depicted in the upper panel, and the coefficients of acceleration noises and optical metrology noises for the PSD and cross-spectral density (CSD) are provided in Table II and III in the Appendix. The separated illustrations of optical metrology noise and acceleration noise in three TDI channels are presented in Fig. 10. As aforementioned, the CFs of $U\bar{U}$ and $A_{U\bar{U}}/E_{U\bar{U}}$ occur around integral multiples of $1/L = 0.12 \text{ Hz}$. In addition to these shared CFs, the $T_{U\bar{U}}$ has extra CFs, with the lowest frequency being $1/(8L) \simeq 0.015 \text{ Hz}$.

The averaged GW responses over all sky directions at a given time are depicted in the middle panel of Fig. 4.

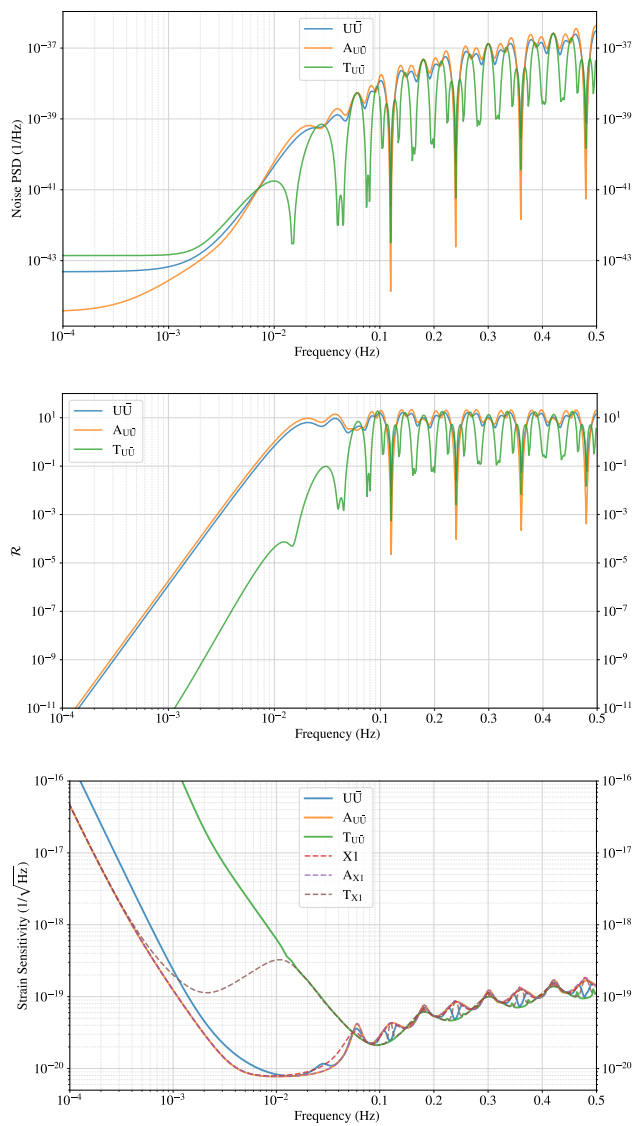


FIG. 4. The noise PSDs (upper), average GW responses over sky directions (middle), and average sensitivities (lower) of hybrid Relay TDI channels. An average sensitivity is obtained by weighting the noise PSD with the corresponding GW response, $\sqrt{\text{PSD}/\mathcal{R}}$.

As observed from the plot, the CFs in the responses align with the noise PSD. In comparison to the other two observables, the response of $T_{U\bar{U}}$ is significantly poorer for frequencies lower than 50 mHz, and the response becomes comparable at higher frequencies. The average sensitivities are obtained by weighting the noise PSD with GW response, $\sqrt{\text{PSD}/\mathcal{R}}$, and the curves are shown in the lower panel of Fig. 4. We emphasize that these sensitivities are instantaneous, the noise PSD and the response are calculated at a selected time point, the spikes of CFs in the PSDs and responses could counteracted numerically. In a realistic scenario, the noise PSD is estimated from a chunk of data during the detector’s orbit, and

the actual response to a specific source varies with time, resulting in time-dependent sensitivities.

The sensitivities of fiducial Michelson TDI channels are also calculated and depicted using dashed curves for comparison. The sensitivities of $A_{U\bar{U}}$ and A_{X1} are identical, and the E channels from different TDI configurations are also expected to be equal. However, the sensitivities of T differ from the science channels. In the frequency band higher than 50 mHz, the $T_{U\bar{U}}$ could be slightly more sensitive than other observables. Due to the unequal arm, T_{X1} diverges from $T_{U\bar{U}}$ at 15 mHz and becomes as sensitive as the A/E for frequencies lower than 0.3 mHz, as analyzed in [40].

IV. SIMULATION AND ANALYSIS

A. Data simulation

The data simulation is performed by using SATDI [29]. Noise data are generated with a sampling rate of 4 Hz for 30 days, and TDI is implemented by using interpolation [41]. The noise sources include acceleration noises and optical metrology noise by assuming that laser noise and clock noise are sufficiently suppressed. Simulations are carried out for second-generation Michelson (X1, Y1, Z1) and hybrid Relay ($U\bar{U}$, $V\bar{V}$, $W\bar{W}$). Optimal observables are generated by using Eq. (6) and employed to evaluate their analytical capabilities.

The GW signals of MBBH are calculated for 25 days preceding their coalescences. Two sources are simulated with different masses: source1 is a binary with $m_1 = 6 \times 10^5 M_\odot$ and $m_2 = 10^5 M_\odot$ in the source frame, and source2 is less massive with $m_1 = 1.2 \times 10^4 M_\odot$ and $m_2 = 2 \times 10^3 M_\odot$. The GW signal of source1 evolves from 0.2 mHz to 20 mHz in 25 days in the detector frame, and the chirp of source2 lasts from 2.3 mHz to 0.5 Hz. These two sources correspond to the signals in the low- and high-frequency bands, respectively. The spins of the black holes are ignored in this simulation. Both two binaries are assumed to originate from an ecliptic longitude $\lambda = 4.6032$ rad and ecliptic longitude $\beta = \pi/10$ rad at redshift $z = 1$, corresponding to a luminosity distance of $d_L = 6791.8$ Mpc [42, 43]. The polarization angle is set to be $\psi = 0.55$ rad, and the inclination angle between the binaries’ rotation and the line-of-sight is $\iota = \pi/3$. The merger time t_c is set to be at the 56th day of mission orbit with reference phase ϕ_c . The time-domain waveforms are generated by using the SEOBNRv4HM model [44].

The waveforms of source2 approaching the merger are depicted in Fig. 5. The x-axis is the barycentric dynamical time (TDB) with respect to the merger at the solar-system barycentric (SSB) center. The grey curve illustrates the GW signal arriving at the SSB center, and the blue and orange curves represent the responded waveforms in A_{X1} and $A_{U\bar{U}}$ observables, respectively. As displayed in the plot, the amplitudes of waveforms are modulated by the TDI response functions. In A_{X1} , the sig-

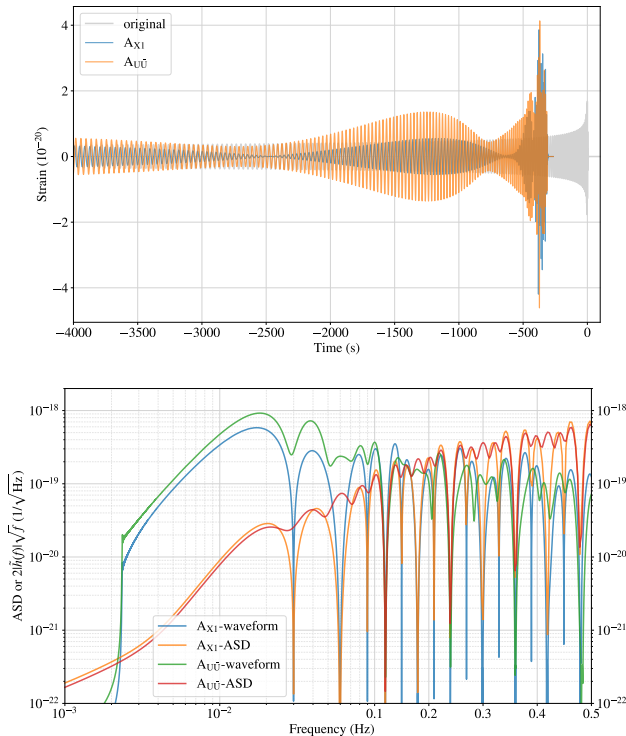


FIG. 5. The time-domain (upper) and frequency-domain (lower) waveforms of source2 ($m_1 = 1.2 \times 10^4 M_\odot$, $m_2 = 2 \times 10^3 M_\odot$) in A_{X1} and $A_{U\bar{U}}$. In the upper plot, the grey curve is the original GW signal arrived at the solar-system barycentric (SSB) center. The x-axis is the barycentric dynamical time with respect to the merger. In current simulation setups and source selection, the merger signal arrives at the detector earlier than it reaches SSB center.

nal amplitude is significantly suppressed around its CFs. Benefiting from the minimal CFs, the waveform in $A_{U\bar{U}}$ is less restrained. Additionally, phase aliasing occurs at high frequencies due to the longer time spans of TDI compared to the GW periods. Frequency-domain waveforms are obtained via Fourier transform and presented in the lower panel of Fig. 5. The noise PSDs of A_{X1} and $A_{U\bar{U}}$ are plotted for comparison, revealing clearer suppression of waveforms at their CFs. In the Michelson observable A_{X1} , the waveform amplitude quickly drops at each CF, as does its PSD. The waveform in $A_{U\bar{U}}$ channel is subjected to a only few CFs.

B. Parameter inferences

The parameters of injected binaries are estimated by using Bayesian algorithm. The inferences are conducted utilizing the optimal observables from second-generation hybrid Relay ($A_{U\bar{U}}$, $E_{U\bar{U}}$, $T_{U\bar{U}}$) and Michelson (A_{X1} , E_{X1} , T_{X1}) to compare their performances. The likeli-

hood function of parameter estimation is given by [45]

$$\ln \mathcal{L}(d|\vec{\theta}) = \sum_{f_i} \left[-\frac{1}{2} (\tilde{\mathbf{d}} - \tilde{\mathbf{h}}(\vec{\theta}))^T \mathbf{C}^{-1} (\tilde{\mathbf{d}} - \tilde{\mathbf{h}}(\vec{\theta}))^* - \frac{1}{2} \ln (\det 2\pi \mathbf{C}) \right], \quad (8)$$

where $\tilde{\mathbf{d}}$ is frequency-domain TDI data obtained via Fourier transform, $\tilde{\mathbf{h}}(\vec{\theta})$ denotes modeled GW signal described by the parameter vector $\vec{\theta} \in [\mathcal{M}_c, q, d_L, \iota, \lambda, \beta, \psi, t_c, \phi_c]$. The responded waveform synthesizes the TDI response function and frequency-domain waveform generated from a reduced-order model of SEOBNRv4HM [46]. The \mathbf{C} is the correlation matrix of noises from three optimal channels,

$$\mathbf{C} = \frac{T_{\text{obs}}}{4} \begin{bmatrix} S_{AA} & S_{AE} & S_{AT} \\ S_{EA} & S_{EE} & S_{ET} \\ S_{TA} & S_{TE} & S_{TT} \end{bmatrix}, \quad (9)$$

where T_{obs} is the duration of data, and PSD S_{xx} and CSD S_{xy} are estimated by using the algorithm detailed in [47]. The priors for parameters are provided in Table I. The redshifted chirp mass $\mathcal{M}_c = (m_1 m_2)^{3/5} / (m_1 + m_2)^{1/5}$ and mass ratio $q = m_2 / m_1$ are inferred instead of inferring individual component masses. The parameter estimations are implemented employing the nested sampler MultiNest [48, 49].

TABLE I. Priors for parameter estimation.

Variable	Prior	range	unit
\mathcal{M}_c	uniform		M_\odot
q	uniform	[0.1, 0.2]	
d_L	Comoving	[5000, 8000]	Mpc
ι	sin	[0, π]	rad
λ	uniform	[0, 2π]	rad
β	cos	$[-\frac{\pi}{2}, \frac{\pi}{2}]$	rad
ψ	uniform	[0, π]	rad
t_c	uniform	$[t_c - 180, t_c + 180]$	second
ϕ_c	uniform	[0, 2π]	rad

The inferred distributions for parameters of source1 are shown in Fig. 6, and results from three TDI combinations are presented. The green colors represent the inferred parameter distributions from ($A_{U\bar{U}}$, $E_{U\bar{U}}$, $T_{U\bar{U}}$), the blue hues signify estimation from (A_{X1} , E_{X1} , T_{X1}), and the magentas depict the result of (A_{X1} , E_{X1}). Among these three combinations, with the exception of (A_{X1} , E_{X1} , T_{X1}), the inferences from other two combinations are consistent, and injected parameters fall within sensible ranges. The discrepancy between (A_{X1} , E_{X1}) and (A_{X1} , E_{X1} , T_{X1}) suggests that the T_{X1} undermines the parameter estimation.

The inferred distributions for source2 are illustrated in Fig. 7. The result from the dataset (A_{X1} , E_{X1} , T_{X1}) noticeably deviates from the injected values. After the T_{X1} data is removed, the science data streams (A_{X1} , E_{X1})

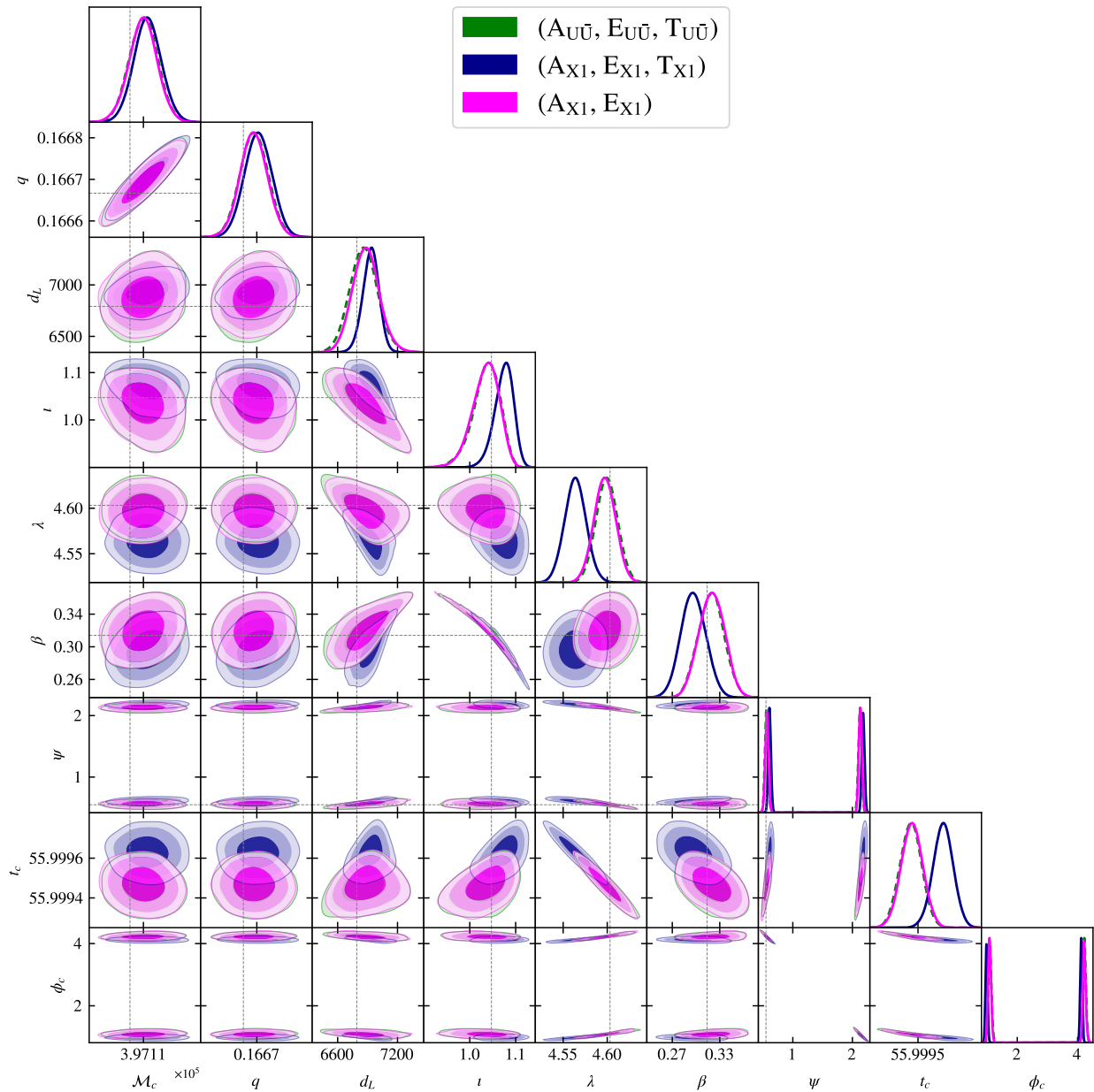


FIG. 6. The inference results for source1 ($m_1 = 6 \times 10^5 M_\odot$ and $m_2 = 10^5 M_\odot$) from three TDI combinations. Three gradients show the 1σ , 2σ , and 3σ regions from darker to lighter.

yield a reasonable result that agrees with the distributions from $(A_{U\bar{U}}, E_{U\bar{U}}, T_{U\bar{U}})$. This further confirms that T_{X1} data is problematic for signal analysis. Additionally, we can notice that inferred mass parameters (M_c , q) are (almost) beyond the credible regions for the $(A_{U\bar{U}}, E_{U\bar{U}}, T_{U\bar{U}})$ group, and this could be caused by the discrepancies between the time-domain waveform model and frequency-domain waveform approximant [50]. For more massive sources1 binary, its waveform has fewer cycles than source2 over the span of 25 days. As a result, the current faithfulness between time-domain waveform and

frequency-domain waveform models may allow for reasonable estimation of the mass parameters for source1, but might not meet the matching requirements for estimating the masses of source2. In the results from two sources, the hybrid Relay demonstrates robust outcomes with its full optimal data set, while the Michelson configuration is susceptible to bias introduced by its T channel. When comparing the results of Michelson across two sources, it appears that source1 exhibits less bias than source2, possibly because the A and E exert greater contributions than the T channel in the low-frequency

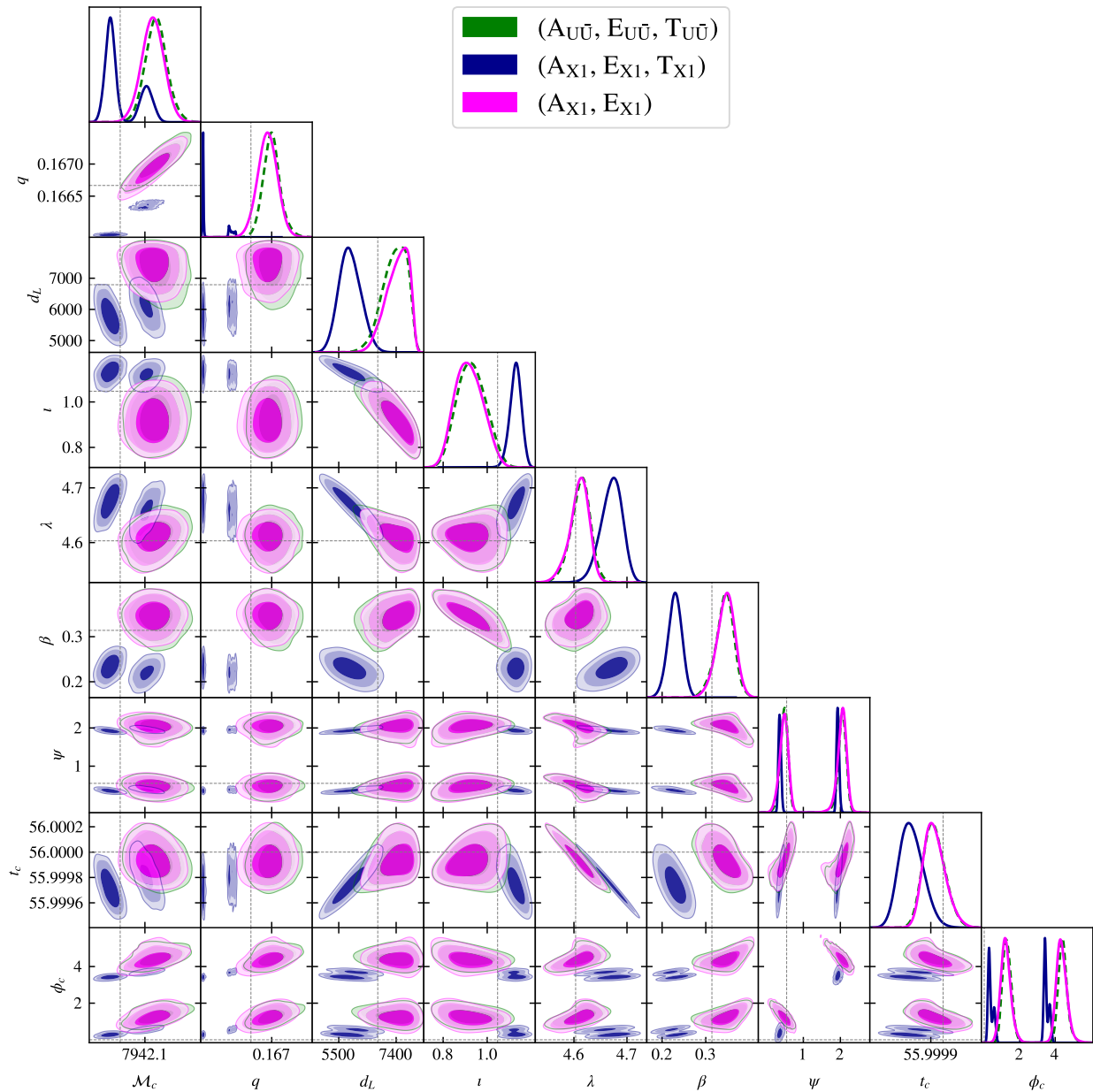


FIG. 7. The corner plots for source2 ($m_1 = 1.2 \times 10^4 M_\odot$, $m_2 = 2 \times 10^3 M_\odot$) from three TDI combinations. Three gradients show the 1σ , 2σ and 3σ regions from darker to lighter.

band.

C. Post-analysis

A further investigation and comparison are performed for the Michelson and hybrid Relay TDI configurations. Three optimal channels utilized are (quasi-)orthogonal. By ignoring their cross-correlations, the determinations of inference from data streams are associated with their

optimal signal-to-noise ratio (SNR) [47],

$$\begin{aligned} \rho_{\text{TDI}}^2 &= 4 \int_0^\infty \frac{|\tilde{h}_{\text{TDI}}(f)|^2}{S_{\text{TDI}}(f)} df \\ &= \int_0^\infty \left(\frac{2|\tilde{h}_{\text{TDI}}(f)|\sqrt{f}}{\sqrt{S_{\text{TDI}}(f)}} \right)^2 d \ln f. \end{aligned} \quad (10)$$

By employing the waveform of source2, the values of $\frac{2|\tilde{h}_{\text{TDI}}(f)|\sqrt{f}}{\sqrt{S_{\text{TDI}}(f)}}$ for the optimal TDI channels are shown in Fig. 8. The upper left panel shows the curves for $(A_{\text{UU}},$

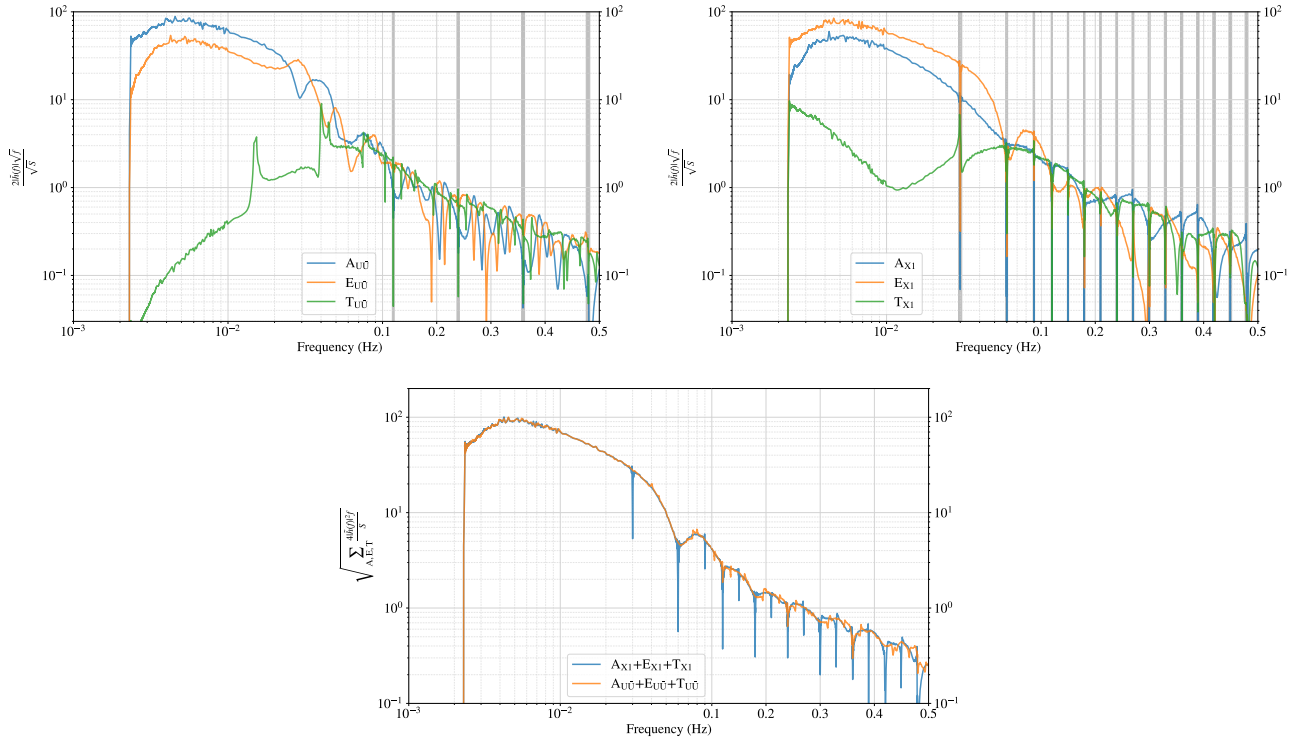


FIG. 8. The ratio $\frac{2|\tilde{h}(f)|\sqrt{f}}{\sqrt{S}}$ for source2 in the optimal TDI channels. The upper left shows the ratios from $(A_{U\bar{U}}, E_{U\bar{U}}, T_{U\bar{U}})$, the upper right is the result from (A_{X1}, E_{X1}, T_{X1}) , and their CFs are marked by grey vertical lines. The lower plot is the square root of quadratic sums of optimal data streams. (In principle, the plots should use a log-scale x-axis to reflect the SNR contributions at different frequencies, the linear scale is utilized at high frequencies to show the CFs more clearly.)

$E_{U\bar{U}}, T_{U\bar{U}}$), and the upper right plot presents the results for (A_{X1}, E_{X1}, T_{X1}) . Grey vertical lines mark the CFs of each TDI configuration. The curves illustrate the science channels, A and E, dominate the SNR in the lower frequencies. The $T_{U\bar{U}}$ makes a trivial contribution in the low frequency band, while the T_{X1} exhibits a moderate SNR contribution in the same range. Our previous analysis showed that this gain is produced by the difference between the ordinary channels (X1, Y1, Z1). In other words, the signal in T_{X1} is from the imperfect cancellation of X1, Y1, and Z1 [40]. That means T_{X1} is susceptible to variations in interferometer arms over time. As a consequence, the T channel from the Michelson configuration not only faces intrinsic larger uncertainty from changing arm lengths due to orbital motion but also has instability in its response function to GW. In this analysis, PSDs are estimated by averaging data over 30 days, leading to inaccurate estimations introduced in T_{X1} . As a result, including the T_{X1} data stream biased the inference results.

In the higher frequency band, the ratios shapely drop at the CFs due to significant suppression of the GW signal and the overestimation of PSD at the CFs caused by smoothing of averaging. The hybrid Relay family is subject to minimal CFs, and the second-generation Michelson suffers from more CFs. To compare the joint SNR

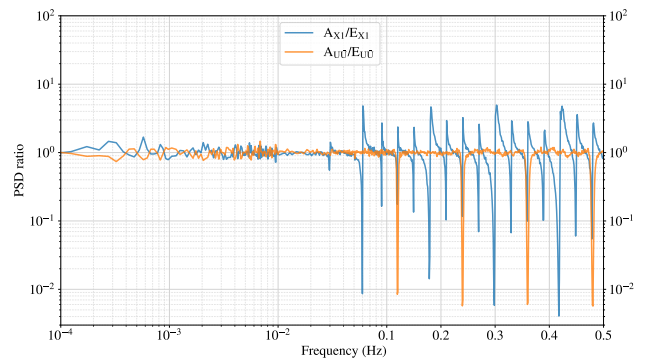


FIG. 9. The PSD ratios of A and E channels for Michelson (blue) and hybrid Relay (orange) configurations. The discontinuities in the ratio of Michelson indicate that the CFs of A_{X1} and E_{X1} are slightly different resulting from the different unequal arms involved in the channels. The PSDs from $A_{U\bar{U}}$ and $E_{U\bar{U}}$ are more identical and stable in the sensitive band except at their CFs.

from three observables, the square root of quadratic sums over A, E, and T, $\sqrt{\sum_{A,E,T} \frac{4|\tilde{h}(f)|^2 f}{S}}$, are calculated and shown in the lower panel. The curve of hybrid Relay configuration is smoother and more robust, whereas the

Michelson observables may slightly lose SNR around the CFs.

For the Michelson channels, another potential problem is the slight difference in CFs between the science channels, A and E. The PSD ratios of A and E, S_A/S_E , for Michelson and hybrid Relay, are depicted in Fig. 9. Below 50 mHz, the PSD of A_{X1} and E_{X1} are closely equal, but as the frequency increase, their PSDs diverge especially around their CFs. In this data chunk, the CF of A_{X1} is slightly lower than E_{X1} which causes the ratio jumps from low to high at each CF. The rhythm of CFs in the hybrid Relay is more stable, the two channels have the same CFs. The ratios are dropped at each CF due to the PSD of $A_{U\bar{U}}$ is lower than the $E_{U\bar{U}}$'s in current case. The asynchronous CFs in Michelson result from the different unequal arms involved in the channels. Optimal observables from the hybrid Relay have the same CFs, potentially enhancing the stability of their covariance matrix and thus benefiting the robustness of data analysis.

V. CONCLUSION AND DISCUSSION

In this work, we present a hybrid Relay second-generation TDI configuration with minimal characteristic frequencies. We compare its capability to the fiducial second-generation TDI Michelson configuration, focusing on laser noise suppression, clock noise cancellation, and GW signal inference as crucial aspects. To evaluate their performance in data analysis, we simulate and analyze data containing GW signals from massive binary black holes. The results demonstrate that new TDI observables effectively satisfy the requirements for laser noise and clock noise suppressions as the Michelson configuration. The hybrid Relay configuration also exhibits robust performance in parameter inference, with noise spectra and GW response function less modulated benefiting from fewer characteristic frequencies. In contrast, the TDI observables from the Michelson configuration would suffer from unequal arm lengths during orbit motion, particularly affecting the T channel at low frequencies which undermines parameter inference. Additionally, the Michelson observables will suffer from more characteristic frequencies where GW signals and noises are significantly suppressed. On the other side, other TDI configurations with asymmetric geometries could also have minimal characteristic frequencies, for instance, the PD observable from mixed Beacon and Monitor as described in [32]. The hybrid Relay should be one of the most straightforward options to implement and readily compatible with current noise solutions of the fiducial Michelson configuration.

We specifically focus on GW signals from massive binary black holes to illustrate our analysis. The science data streams, A and E, dominate the inference outcome, and the T channel is insignificant and negligible in the

analysis for such sources. However, the T observable, being noise-dominant, is crucial for characterizing instrumental noises and separating stochastic GW [51–53]. The T data from Michelson is susceptible to time-varying arms and contamination by GW signal, rendering it ineligible for this task. The T channel from the hybrid Relay, being genuinely noise-dominating data, could be more suitable for noise characterization. On the other side, the selected chirp signal quickly sweeps over the high frequency band which weakens the impacts of characteristic frequencies. For a slowly evolved GW signal, such as the early inspiral of stellar mass binaries, the signal will last much longer around TDI's characteristic frequencies, and then the signal will be dramatically suppressed and modulated. Observables with fewer null frequencies will promote signal recoveries by reducing modulations and suppressions.

Machine learning techniques have been employed to boost the efficiency of GW identifications and estimations [54–62, and reference therein]. The concept of global fits has been proposed to simultaneously resolve various GW signals [63, 64]. TDI observables with stable PSDs and GW response functions are essential for these analyses. The proposed hybrid Relay could be the eligible configuration to fulfill these requirements, and we are committed to further studies in future work.

ACKNOWLEDGMENTS

GW was supported by the National Key R&D Program of China under Grant No. 2021YFC2201903, and NSFC No. 12003059. This work made use of the High Performance Computing Resource in the Core Facility for Advanced Research Computing at Shanghai Astronomical Observatory. This work are performed by using the python packages `numpy` [65], `scipy` [66], `pandas` [67], `PyCBC` [68, 69], `LALSuite` [70, 71], `astropy` [43], `BILBY` [72], `MultiNest` [48] and `PyMultiNest` [49], and the plots are make by utilizing `matplotlib` [73], `GetDist` [74].

Appendix A: PSD and CSD of hybrid Relay TDI observables

The PSDs of secondary noises separating the acceleration noise and optical metrology noise are depicted in Fig. 10. The coefficients of acceleration noises and optical metrology noises for both PSD and CSD are provided in Tables II and III, respectively. In the $U\bar{U}$ channel, optical metrology noise predominates over acceleration except within the frequency range of [1, 4] mHz. In the $A_{U\bar{U}}$ channels, acceleration noise surpasses optical path noise in the lower frequency band, while optical noise becomes a dominant factor at higher frequencies. In the $T_{U\bar{U}}$ channel, optical metrology noise overwhelms acceleration noise across the entire frequency band.

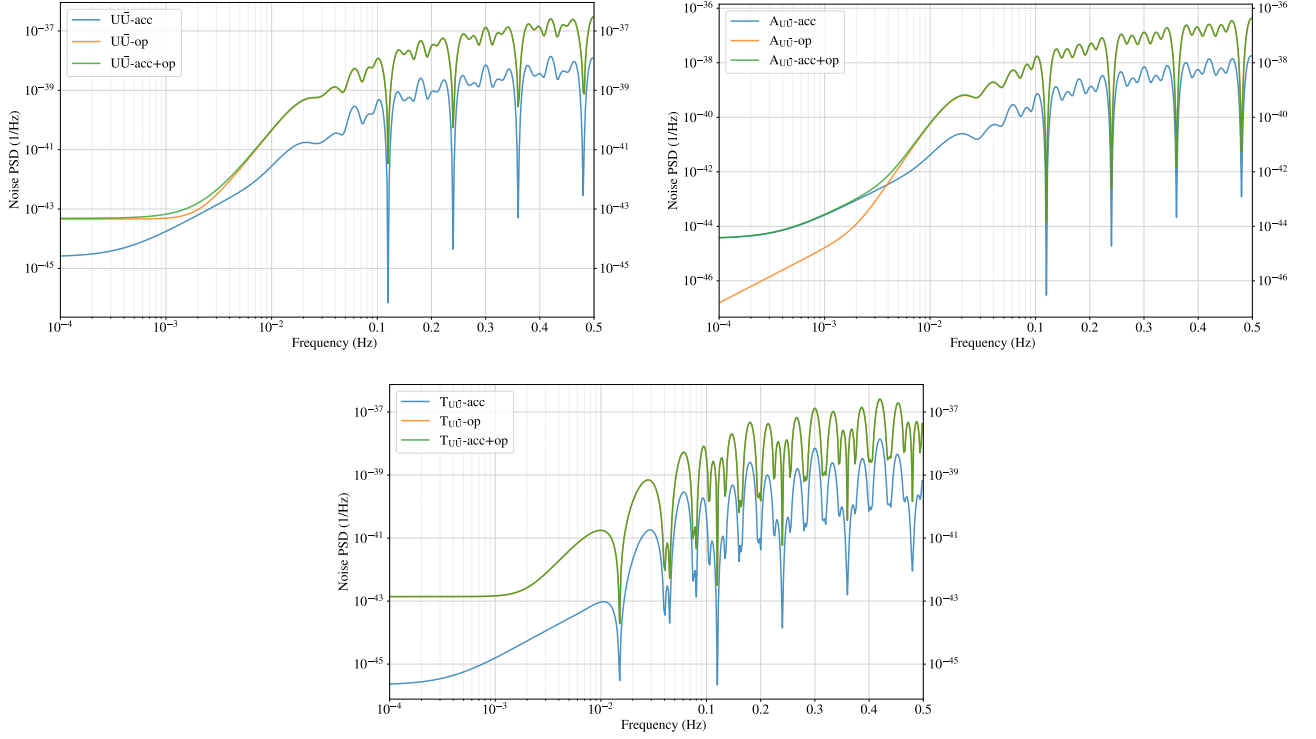


FIG. 10. The PSDs of $U_{\bar{U}}$, $A_{\bar{U}}$, and $T_{\bar{U}}$ observables with separating acceleration noises (acc) and optical metrology noises (op). In the $U_{\bar{U}}$ channel, optical metrology noise dominates over acceleration except within the range of [1, 4] mHz. The acceleration noise is higher than the optical path noise in low frequencies for $A_{\bar{U}}$, and optical noise becomes the dominant noise in higher frequencies. In the $T_{\bar{U}}$ channel, the optical metrology noise overwhelms acceleration noise across the entire frequency band.

-
- [1] P. Amaro-Seoane, H. Audley, S. Babak, and et al (LISA Team), Laser Interferometer Space Antenna, arXiv e-prints, arXiv:1702.00786 (2017).
- [2] M. Colpi *et al.*, LISA Definition Study Report, (2024), arXiv:2402.07571 [astro-ph.CO].
- [3] J. W. Armstrong, F. B. Estabrook, and M. Tinto, Time-Delay Interferometry for Space-based Gravitational Wave Searches, *Astrophys. J.* **527**, 814 (1999).
- [4] F. B. Estabrook, M. Tinto, and J. W. Armstrong, Time-delay analysis of LISA gravitational wave data: Elimination of spacecraft motion effects, *Phys. Rev. D* **62**, 042002 (2000).
- [5] J. W. Armstrong, F. B. Estabrook, and M. Tinto, Sensitivities of alternate LISA configurations, *Classical and Quantum Gravity* **18**, 4059 (2001).
- [6] S. L. Larson, R. W. Hellings, and W. A. Hiscock, Unequal arm space borne gravitational wave detectors, *Phys. Rev. D* **66**, 062001 (2002), arXiv:gr-qc/0206081.
- [7] S. V. Dhurandhar, K. Rajesh Nayak, and J. Y. Vinet, Algebraic approach to time-delay data analysis for LISA, *Phys. Rev. D* **65**, 102002 (2002), arXiv:gr-qc/0112059 [gr-qc].
- [8] M. Tinto, D. A. Shaddock, J. Sylvestre, and J. W. Armstrong, Implementation of time-delay interferometry for LISA, *Phys. Rev. D* **67**, 122003 (2003), arXiv:gr-qc/0303013 [gr-qc].
- [9] M. Vallisneri, Synthetic LISA: Simulating time delay interferometry in a model LISA, *Phys. Rev. D* **71**, 022001 (2005), arXiv:gr-qc/0407102 [gr-qc].
- [10] A. Petiteau, G. Auger, H. Halloin, O. Jeannin, E. Plagnol, S. Pireaux, T. Regimbau, and J.-Y. Vinet, LISACode: A scientific simulator of LISA, *Phys. Rev. D* **77**, 023002 (2008), arXiv:0802.2023 [gr-qc].
- [11] M. Tinto and S. V. Dhurandhar, Time-delay interferometry, *Living Rev. Rel.* **24**, 1 (2021).
- [12] D. A. Shaddock, M. Tinto, F. B. Estabrook, and J. Armstrong, Data combinations accounting for LISA spacecraft motion, *Phys. Rev. D* **68**, 061303 (2003), arXiv:gr-qc/0307080.
- [13] N. J. Cornish and R. W. Hellings, The Effects of orbital motion on LISA time delay interferometry, *Class. Quant. Grav.* **20**, 4851 (2003), arXiv:gr-qc/0306096 [gr-qc].
- [14] M. Tinto, F. B. Estabrook, and J. Armstrong, Time delay interferometry with moving spacecraft arrays, *Phys. Rev. D* **69**, 082001 (2004), arXiv:gr-qc/0310017.
- [15] S. Dhurandhar, K. Nayak, and J. Vinet, Time Delay Interferometry for LISA with one arm dysfunctional, *Class. Quant. Grav.* **27**, 135013 (2010), arXiv:1001.4911 [gr-qc].
- [16] J.-B. Bayle, M. Lilley, A. Petiteau, and H. Halloin, Effect of filters on the time-delay interferometry residual

TABLE II. The coefficients of noise components for PSD (power-spectral density) of $U\bar{U}$ and their optimal TDI channels ($x = 2\pi fL$).

	$U\bar{U}$	$A_{U\bar{U}}$
S_{acc12}	$64 \cos^2 x \sin^4 x$	$32 \cos^2 x (5 + 6 \cos x)^2 \sin^4 \frac{x}{2}$
S_{acc21}	$16 \sin^4 x$	$32 \sin^4 \frac{x}{2} (5 \cos x + 2 \cos 2x + \cos 3x + 3)^2$
S_{acc13}	$64 \cos^2 x \sin^4 x$	$8 \sin^4 x (1 - 2 \cos x)^2$
S_{acc31}	$16(1 + 2 \cos 2x)^2 \sin^4 x$	$8 \sin^4 x (-2 \cos x + 2 \cos 2x + 1)^2$
S_{acc23}	$64 \cos^2 x (3 + 4 \cos x)^2 \sin^4 \frac{x}{2}$	$32 \sin^4 \frac{x}{2} (5 \cos x + 2 \cos 2x + \cos 3x + 3)^2$
S_{acc32}	$64 \cos^2 x \sin^4 \frac{3x}{2}$	$32 \sin^4 \frac{3x}{2} (6 \cos x + 3 \cos 2x + \cos 3x + 3)^2$
S_{op12}	$4 \sin^2 x$	$8 \sin^4 \frac{x}{2} (46 \cos x + 30 \cos 2x + 14 \cos 3x + 4 \cos 4x + 27)$
S_{op21}	$4 \sin^2 x$	$8 \sin^4 \frac{x}{2} (46 \cos x + 30 \cos 2x + 14 \cos 3x + 4 \cos 4x + 27)$
S_{op13}	$4 \sin^2 x$	$8 \sin^2 \frac{x}{2} \sin^2 x$
S_{op31}	$4 \sin^2 x$	$8 \sin^2 \frac{x}{2} \sin^2 x$
S_{op23}	$2(2 - \cos x + \cos 2x - 2 \cos 3x - \cos 5x + \cos 6x)$	$8 \sin^4 \frac{x}{2} (58 \cos x + 42 \cos 2x + 24 \cos 3x + 10 \cos 4x + 2 \cos 5x + 33)$
S_{op32}	$2(2 - \cos x + \cos 2x - 2 \cos 3x - \cos 5x + \cos 6x)$	$8 \sin^4 \frac{x}{2} (58 \cos x + 42 \cos 2x + 24 \cos 3x + 10 \cos 4x + 2 \cos 5x + 33)$
	$T_{U\bar{U}}$	$E_{U\bar{U}}$
S_{acc12}	$\frac{64}{3} \sin^4 \frac{x}{2} (\cos x + \cos 2x + \cos 3x)^2$	$\frac{32}{3} \sin^4 \frac{x}{2} (5 \cos x + 5 \cos 2x + 2 \cos 3x + 3)^2$
S_{acc21}	$\frac{64}{3} \sin^4 \frac{x}{2} (\cos x + \cos 2x + \cos 3x)^2$	$\frac{32}{3} \sin^4 \frac{x}{2} (7 \cos x + 4 \cos 2x + \cos 3x + 3)^2$
S_{acc13}	$\frac{64}{3} \sin^4 \frac{x}{2} (\cos x + \cos 2x + \cos 3x)^2$	$\frac{32}{3} \sin^4 \frac{x}{2} (11 \cos x + 5 \cos 2x + 2 \cos 3x + 6)^2$
S_{acc31}	$\frac{64}{3} \sin^4 \frac{x}{2} (\cos x + \cos 2x + \cos 3x)^2$	$\frac{32}{3} \sin^4 \frac{x}{2} (10 \cos x + 7 \cos 2x + \cos 3x + 6)^2$
S_{acc23}	$\frac{64}{3} \sin^4 \frac{x}{2} (\cos x + \cos 2x + \cos 3x)^2$	$\frac{32}{3} \sin^4 \frac{x}{2} (5 \cos x + 2 \cos 2x - \cos 3x + 3)^2$
S_{acc32}	$\frac{64}{3} \sin^4 \frac{x}{2} (\cos x + \cos 2x + \cos 3x)^2$	$\frac{32}{3} \sin^4 \frac{x}{2} (4 \cos x + \cos 2x + \cos 3x + 3)^2$
S_{op12}	$\frac{4}{3} (\sin \frac{x}{2} - \sin \frac{7x}{2})^2$	$\frac{8}{3} \sin^4 \frac{x}{2} (74 \cos x + 54 \cos 2x + 34 \cos 3x + 16 \cos 4x + 4 \cos 5x + 43)$
S_{op21}	$\frac{4}{3} (\sin \frac{x}{2} - \sin \frac{7x}{2})^2$	$\frac{8}{3} \sin^4 \frac{x}{2} (74 \cos x + 54 \cos 2x + 34 \cos 3x + 16 \cos 4x + 4 \cos 5x + 43)$
S_{op13}	$\frac{4}{3} (\sin \frac{x}{2} - \sin \frac{7x}{2})^2$	$\frac{16}{3} \sin^4 \frac{x}{2} (103 \cos x + 72 \cos 2x + 38 \cos 3x + 14 \cos 4x + 2 \cos 5x + 59)$
S_{op31}	$\frac{4}{3} (\sin \frac{x}{2} - \sin \frac{7x}{2})^2$	$\frac{16}{3} \sin^4 \frac{x}{2} (103 \cos x + 72 \cos 2x + 38 \cos 3x + 14 \cos 4x + 2 \cos 5x + 59)$
S_{op23}	$\frac{4}{3} (\sin \frac{x}{2} - \sin \frac{7x}{2})^2$	$\frac{8}{3} \sin^4 \frac{x}{2} (38 \cos x + 18 \cos 2x + 4 \cos 3x - 2 \cos 4x - 2 \cos 5x + 25)$
S_{op32}	$\frac{4}{3} (\sin \frac{x}{2} - \sin \frac{7x}{2})^2$	$\frac{8}{3} \sin^4 \frac{x}{2} (38 \cos x + 18 \cos 2x + 4 \cos 3x - 2 \cos 4x - 2 \cos 5x + 25)$

laser noise for LISA, Phys. Rev. D **99**, 084023 (2019), arXiv:1811.01575 [astro-ph.IM].

- [17] M. Muratore, D. Vetrugno, and S. Vitale, Revisitation of time delay interferometry combinations that suppress laser noise in LISA, arXiv e-prints (2020), arXiv:2001.11221 [astro-ph.IM].
- [18] M. Tinto, S. Dhurandhar, and D. Malakar, Second-generation time-delay interferometry, Phys. Rev. D **107**, 082001 (2023), arXiv:2212.05967 [gr-qc].
- [19] M. Vallisneri, J.-B. Bayle, S. Babak, and A. Petiteau, TDI-infinity: time-delay interferometry without delays, (2020), arXiv:2008.12343 [gr-qc].
- [20] J. Page and T. B. Littenberg, Bayesian time delay interferometry, Phys. Rev. D **104**, 084037 (2021), arXiv:2107.08174 [gr-qc].
- [21] J. Page and T. B. Littenberg, Bayesian time delay interferometry for orbiting LISA: Accounting for the time dependence of spacecraft separations, Phys. Rev. D **108**, 044065 (2023), arXiv:2305.14186 [gr-qc].
- [22] Q. Baghi, J. I. Thorpe, J. Slutsky, and J. Baker, Statistical inference approach to time-delay interferometry for gravitational-wave detection, Phys. Rev. D **103**, 042006 (2021), arXiv:2010.07224 [gr-qc].
- [23] Q. Baghi, J. G. Baker, J. Slutsky, and J. I. Thorpe, Fully Data-Driven Time-Delay Interferometry with Time-Varying Delays, Annalen Phys. **536**, 2200447 (2024), arXiv:2209.10851 [gr-qc].
- [24] M. Otto, G. Heinzel, and K. Danzmann, TDI and clock noise removal for the split interferometry configuration of LISA, Class. Quant. Grav. **29**, 205003 (2012).
- [25] M. Otto, Time-Delay Interferometry Simulations for the Laser Interferometer Space Antenna (2015).
- [26] M. Tinto and O. Hartwig, Time-Delay Interferometry and Clock-Noise Calibration, Phys. Rev. D **98**, 042003 (2018), arXiv:1807.02594 [gr-qc].
- [27] O. Hartwig and J.-B. Bayle, Clock-jitter reduction in LISA time-delay interferometry combinations, Phys. Rev. D **103**, 123027 (2021), arXiv:2005.02430 [astro-ph.IM].
- [28] O. Hartwig, *Instrumental modelling and noise reduction algorithms for the Laser Interferometer Space Antenna*, Ph.D. thesis, Leibniz U., Hannover (2021).
- [29] G. Wang, SATDI: Simulation and Analysis for Time-Delay Interferometry, (2024), arXiv:2403.xxxx [gr-qc].
- [30] W.-T. Ni, J.-T. Shy, S.-M. Tseng, X. Xu, H.-C. Yeh, W.-Y. Hsu, W.-L. Liu, S.-D. Tzeng, P. Fridelance, E. Samain, D. Lee, Z.-Y. Su, and A.-M. Wu, Progress in mission concept study and laboratory development for the ASTROD (Astrodynamical Space Test of Relativity using Optical Devices), in *Small Spacecraft, Space Environments, and Instrumentation Technologies*, Society of Photo-Optical Instrumentation Engineers (SPIE) Conference Series, Vol. 3116, edited by F. A. Allahdadi, E. K. Casani, and T. D. Maclay (1997) pp. 105–116.
- [31] G. Wang, Time-delay Interferometry for ASTROD-GW (2011).
- [32] G. Wang, W.-T. Ni, W.-B. Han, and C.-F. Qiao, Algorithm for time-delay interferometry numerical simulation

- and sensitivity investigation, *Phys. Rev. D* **103**, 122006 (2021), arXiv:2010.15544 [gr-qc].
- [33] M. Vallisneri, Geometric time delay interferometry, *Phys. Rev. D* **72**, 042003 (2005), [Erratum: *Phys. Rev. D* **76**, 109903(2007)], arXiv:gr-qc/0504145 [gr-qc].
- [34] O. Hartwig and M. Muratore, Characterization of time delay interferometry combinations for the LISA instrument noise, *Phys. Rev. D* **105**, 062006 (2022), arXiv:2111.00975 [gr-qc].
- [35] T. A. Prince, M. Tinto, S. L. Larson, and J. W. Armstrong, The LISA optimal sensitivity, *Phys. Rev. D* **66**, 122002 (2002), arXiv:gr-qc/0209039 [gr-qc].
- [36] G. Wang and W.-T. Ni, Numerical simulation of time delay interferometry for TAIJI and new LISA, *Res. Astron. Astrophys.* **19**, 058 (2019), arXiv:1707.09127 [astro-ph.IM].
- [37] G. Wang, W.-T. Ni, W.-B. Han, S.-C. Yang, and X.-Y. Zhong, Numerical simulation of sky localization for LISA-TAIJI joint observation, *Phys. Rev. D* **102**, 024089 (2020), arXiv:2002.12628.
- [38] J.-B. Bayle and O. Hartwig, Unified model for the LISA measurements and instrument simulations, *Phys. Rev. D* **107**, 083019 (2023), arXiv:2212.05351 [gr-qc].
- [39] M. Staab, M. Lilley, J.-B. Bayle, and O. Hartwig, Laser noise residuals in LISA from onboard processing and time-delay interferometry, (2023), arXiv:2306.11774 [astro-ph.IM].
- [40] G. Wang and W.-T. Ni, Revisiting time delay interferometry for unequal-arm LISA and TAIJI, *Phys. Scripta* **98**, 075005 (2023), arXiv:2008.05812 [gr-qc].
- [41] D. A. Shaddock, B. Ware, R. E. Spero, and M. Vallisneri, Post-processed time-delay interferometry for LISA, *Phys. Rev. D* **70**, 081101 (2004), arXiv:gr-qc/0406106.
- [42] N. Aghanim *et al.* (Planck), Planck 2018 results. VI. Cosmological parameters, *Astron. Astrophys.* **641**, A6 (2020), [Erratum: *Astron. Astrophys.* **652**, C4 (2021)], arXiv:1807.06209 [astro-ph.CO].
- [43] T. P. Robitaille *et al.* (Astropy), Astropy: A Community Python Package for Astronomy, *Astron. Astrophys.* **558**, A33 (2013), arXiv:1307.6212 [astro-ph.IM].
- [44] A. Bohé *et al.*, Improved effective-one-body model of spinning, nonprecessing binary black holes for the era of gravitational-wave astrophysics with advanced detectors, *Phys. Rev. D* **95**, 044028 (2017), arXiv:1611.03703 [gr-qc].
- [45] J. D. Romano and N. J. Cornish, Detection methods for stochastic gravitational-wave backgrounds: a unified treatment, *Living Rev. Rel.* **20**, 2 (2017), arXiv:1608.06889 [gr-qc].
- [46] R. Cotesta, S. Marsat, and M. Pürrer, Frequency domain reduced order model of aligned-spin effective-one-body waveforms with higher-order modes, *Phys. Rev. D* **101**, 124040 (2020), arXiv:2003.12079 [gr-qc].
- [47] B. Allen, W. G. Anderson, P. R. Brady, D. A. Brown, and J. D. E. Creighton, FINDCHIRP: An Algorithm for detection of gravitational waves from inspiraling compact binaries, *Phys. Rev. D* **85**, 122006 (2012), arXiv:gr-qc/0509116.
- [48] F. Feroz, M. P. Hobson, and M. Bridges, MultiNest: an efficient and robust Bayesian inference tool for cosmology and particle physics, *Mon. Not. Roy. Astron. Soc.* **398**, 1601 (2009), arXiv:0809.3437 [astro-ph].
- [49] J. Buchner, A. Georgakakis, K. Nandra, L. Hsu, C. Rangel, M. Brightman, A. Merloni, M. Salvato, J. Donley, and D. Kocevski, X-ray spectral modelling of the AGN obscuring region in the CDFS: Bayesian model selection and catalogue, *Astron. Astrophys.* **564**, A125 (2014), arXiv:1402.0004 [astro-ph.HE].
- [50] C. Cutler and M. Vallisneri, LISA detections of massive black hole inspirals: Parameter extraction errors due to inaccurate template waveforms, *Phys. Rev. D* **76**, 104018 (2007), arXiv:0707.2982 [gr-qc].
- [51] G. Wang, B. Li, P. Xu, and X. Fan, Characterizing instrumental noise and stochastic gravitational wave signals from combined time-delay interferometry, *Phys. Rev. D* **106**, 044054 (2022), arXiv:2201.10902 [gr-qc].
- [52] M. Muratore, O. Hartwig, D. Vetrugno, S. Vitale, and W. J. Weber, Effectiveness of null time-delay interferometry channels as instrument noise monitors in LISA, *Phys. Rev. D* **107**, 082004 (2023), arXiv:2207.02138 [gr-qc].
- [53] O. Hartwig, M. Lilley, M. Muratore, and M. Pieroni, Stochastic gravitational wave background reconstruction for a nonequilateral and unequal-noise LISA constellation, *Phys. Rev. D* **107**, 123531 (2023), arXiv:2303.15929 [gr-qc].
- [54] M. J. Williams, J. Veitch, and C. Messenger, Nested sampling with normalizing flows for gravitational-wave inference, *Phys. Rev. D* **103**, 103006 (2021), arXiv:2102.11056 [gr-qc].
- [55] H. Gabbard, C. Messenger, I. S. Heng, F. Tonolini, and R. Murray-Smith, Bayesian parameter estimation using conditional variational autoencoders for gravitational-wave astronomy, *Nature Phys.* **18**, 112 (2022), arXiv:1909.06296 [astro-ph.IM].
- [56] J. Langendorff, A. Kolmus, J. Janquart, and C. Van Den Broeck, Normalizing Flows as an Avenue to Studying Overlapping Gravitational Wave Signals, *Phys. Rev. Lett.* **130**, 171402 (2023), arXiv:2211.15097 [gr-qc].
- [57] M. Dax, S. R. Green, J. Gair, M. Pürrer, J. Wildberger, J. H. Macke, A. Buonanno, and B. Schölkopf, Neural Importance Sampling for Rapid and Reliable Gravitational-Wave Inference, *Phys. Rev. Lett.* **130**, 171403 (2023), arXiv:2210.05686 [gr-qc].
- [58] W.-H. Ruan, H. Wang, C. Liu, and Z.-K. Guo, Rapid search for massive black hole binary coalescences using deep learning, *Phys. Lett. B* **841**, 137904 (2023), arXiv:2111.14546 [astro-ph.IM].
- [59] W. Ruan, H. Wang, C. Liu, and Z. Guo, Parameter Inference for Coalescing Massive Black Hole Binaries Using Deep Learning, *Universe* **9**, 407 (2023), arXiv:2307.14844 [astro-ph.IM].
- [60] M. Du, B. Liang, H. Wang, P. Xu, Z. Luo, and Y. Wu, Advancing Space-Based Gravitational Wave Astronomy: Rapid Detection and Parameter Estimation Using Normalizing Flows, (2023), arXiv:2308.05510 [astro-ph.IM].
- [61] T.-Y. Sun, C.-Y. Xiong, S.-J. Jin, Y.-X. Wang, J.-F. Zhang, and X. Zhang, Efficient parameter inference for gravitational wave signals in the presence of transient noises using normalizing flow, (2023), arXiv:2312.08122 [gr-qc].
- [62] Y. Xu, M. Du, P. Xu, B. Liang, and H. Wang, Gravitational Wave Signal Extraction Against Non-Stationary Instrumental Noises with Deep Neural Network, (2024), arXiv:2402.13091 [gr-qc].
- [63] T. Littenberg, N. Cornish, K. Lackeos, and T. Robson, Global Analysis of the Gravitational Wave Signal from Galactic Binaries, *Phys. Rev. D* **101**, 123021 (2020),

- arXiv:2004.08464 [gr-qc].
- [64] T. B. Littenberg and N. J. Cornish, Prototype global analysis of LISA data with multiple source types, *Phys. Rev. D* **107**, 063004 (2023), arXiv:2301.03673 [gr-qc].
- [65] C. R. Harris, K. J. Millman, S. J. van der Walt, R. Gommers, P. Virtanen, D. Cournapeau, E. Wieser, J. Taylor, S. Berg, N. J. Smith, R. Kern, M. Picus, S. Hoyer, M. H. van Kerkwijk, M. Brett, A. Haldane, J. F. del Río, M. Wiebe, P. Peterson, P. Gérard-Marchant, K. Sheppard, T. Reddy, W. Weckesser, H. Abbasi, C. Gohlke, and T. E. Oliphant, Array programming with NumPy, *Nature* **585**, 357 (2020).
- [66] P. Virtanen, R. Gommers, T. E. Oliphant, M. Haberland, T. Reddy, D. Cournapeau, E. Burovski, P. Peterson, W. Weckesser, J. Bright, S. J. van der Walt, M. Brett, J. Wilson, K. J. Millman, N. Mayorov, A. R. J. Nelson, E. Jones, R. Kern, E. Larson, C. J. Carey, Í. Polat, Y. Feng, E. W. Moore, J. VanderPlas, D. Laxalde, J. Perktold, R. Cimrman, I. Henriksen, E. A. Quintero, C. R. Harris, A. M. Archibald, A. H. Ribeiro, F. Pedregosa, P. van Mulbregt, and SciPy 1.0 Contributors, SciPy 1.0: Fundamental Algorithms for Scientific Computing in Python, *Nature Methods* **17**, 261 (2020).
- [67] T. pandas development team, pandas-dev/pandas: Pandas (2020).
- [68] S. A. Usman *et al.*, The PyCBC search for gravitational waves from compact binary coalescence, *Class. Quant. Grav.* **33**, 215004 (2016), arXiv:1508.02357 [gr-qc].
- [69] C. M. Biwer, C. D. Capano, S. De, M. Cabero, D. A. Brown, A. H. Nitz, and V. Raymond, PyCBC Inference: A Python-based parameter estimation toolkit for compact binary coalescence signals, *Publ. Astron. Soc. Pac.* **131**, 024503 (2019), arXiv:1807.10312 [astro-ph.IM].
- [70] LIGO Scientific Collaboration, Virgo Collaboration, and KAGRA Collaboration, LVK Algorithm Library - LALSuite, Free software (GPL) (2018).
- [71] K. Wette, SWIGLAL: Python and Octave interfaces to the LALSuite gravitational-wave data analysis libraries, *SoftwareX* **12**, 100634 (2020).
- [72] G. Ashton *et al.*, BILBY: A user-friendly Bayesian inference library for gravitational-wave astronomy, *Astrophys. J. Suppl.* **241**, 27 (2019), arXiv:1811.02042 [astro-ph.IM].
- [73] J. D. Hunter, Matplotlib: A 2D Graphics Environment, *Comput. Sci. Eng.* **9**, 90 (2007).
- [74] A. Lewis, GetDist: a Python package for analysing Monte Carlo samples, (2019), arXiv:1910.13970 [astro-ph.IM].

TABLE III. The coefficients of noise components for CSD (cross-spectral density) of $U\bar{U}$ and their optimal TDI channels ($x = 2\pi fL$).

	CSD($U\bar{U}, V\bar{V}$)
S_{acc12}	$32 \sin^4 x (2 \cos x + \cos 3x)$
S_{acc21}	$32 \sin^4 x \cos x$
S_{acc13}	$-64 \sin^4 \frac{x}{2} (3 \cos \frac{x}{2} + 2 \cos \frac{3x}{2} + \cos \frac{5x}{2})^2$
S_{acc31}	$2(-\cos 2x + \cos 4x + 2 \cos 5x + \cos 6x - 2 \cos 7x - 1)$
S_{acc23}	$-64 \sin^4 \frac{x}{2} (4 \cos x + 3) (\cos \frac{x}{2} + \cos \frac{3x}{2})^2$
S_{acc32}	$-128 \sin^4 \frac{x}{2} \cos x (2 \cos \frac{x}{2} + \cos \frac{3x}{2})^2$
S_{op12}	$4 \sin^2 x \cos x + 4i \sin^3 x$
S_{op21}	$4 \sin^2 x \cos x - 4i \sin^3 x$
S_{op13}	$(\cos 4x + \cos 5x - \cos 7x - 1) - i(2 \sin x - \sin 4x - \sin 5x + \sin 7x)$
S_{op31}	$(\cos 4x + \cos 5x - \cos 7x - 1) + i(2 \sin x - \sin 4x - \sin 5x + \sin 7x)$
S_{op23}	$4 \sin^2 x (-\cos x + \cos 2x + \cos 4x) + i(\sin x - \sin 2x + \sin 3x + \sin 4x - \sin 6x)$
S_{op32}	$4 \sin^2 x (-\cos x + \cos 2x + \cos 4x) - i(\sin x - \sin 2x + \sin 3x + \sin 4x - \sin 6x)$
	CSD($A_{U\bar{U}}, E_{U\bar{U}}$)
S_{acc12}	$\frac{16}{\sqrt{3}} \sin^4 \frac{x}{2} (106 \cos x + 83 \cos 2x + 52 \cos 3x + 25 \cos 4x + 6 \cos 5x + 58)$
S_{acc21}	$\frac{16}{\sqrt{3}} \sin^4 \frac{x}{2} (112 \cos x + 83 \cos 2x + 46 \cos 3x + 20 \cos 4x + 6 \cos 5x + \cos 6x + 62)$
S_{acc13}	$-\frac{64}{\sqrt{3}} \sin^4 \frac{x}{2} \cos^2 \frac{x}{2} (6 \cos x + 8 \cos 2x + 3 \cos 3x + 2 \cos 4x + 5)$
S_{acc31}	$-\frac{64}{\sqrt{3}} \sin^4 \frac{x}{2} \cos^2 \frac{x}{2} (2 \cos x + 8 \cos 2x + 4 \cos 3x + 6 \cos 4x + \cos 5x + 3)$
S_{acc23}	$\frac{16}{\sqrt{3}} \sin^4 \frac{x}{2} (-88 \cos x - 61 \cos 2x - 30 \cos 3x - 8 \cos 4x + 2 \cos 5x + \cos 6x - 50)$
S_{acc32}	$-\frac{16}{\sqrt{3}} \sin^4 \frac{x}{2} (82 \cos x + 58 \cos 2x + 30 \cos 3x + 13 \cos 4x + 4 \cos 5x + \cos 6x + 46)$
S_{op12}	$\frac{8}{\sqrt{3}} \sin^4 \frac{x}{2} (56 \cos x + 42 \cos 2x + 24 \cos 3x + 10 \cos 4x + 2 \cos 5x + 31) + \frac{i}{\sqrt{3}} (6 \sin x - \sin 2x - \sin 5x - \sin 6x + \sin 7x)$
S_{op21}	$\frac{8}{\sqrt{3}} \sin^4 \frac{x}{2} (56 \cos x + 42 \cos 2x + 24 \cos 3x + 10 \cos 4x + 2 \cos 5x + 31) - \frac{i}{\sqrt{3}} (6 \sin x - \sin 2x - \sin 5x - \sin 6x + \sin 7x)$
S_{op13}	$-\frac{64}{\sqrt{3}} \sin^4 \frac{x}{2} \cos^2 \frac{x}{2} (\cos x + 2 \cos 2x + \cos 3x + \cos 4x + 1) - \frac{i}{\sqrt{3}} (6 \sin x - \sin 2x - \sin 5x - \sin 6x + \sin 7x)$
S_{op31}	$-\frac{64}{\sqrt{3}} \sin^4 \frac{x}{2} \cos^2 \frac{x}{2} (\cos x + 2 \cos 2x + \cos 3x + \cos 4x + 1) + \frac{i}{\sqrt{3}} (6 \sin x - \sin 2x - \sin 5x - \sin 6x + \sin 7x)$
S_{op23}	$-\frac{8}{\sqrt{3}} \sin^4 \frac{x}{2} (2 \cos x + 1)^2 (6 \cos x + 4 \cos 2x + 3) + \frac{i}{\sqrt{3}} (6 \sin x - \sin 2x - \sin 5x - \sin 6x + \sin 7x)$
S_{op32}	$-\frac{8}{\sqrt{3}} \sin^4 \frac{x}{2} (2 \cos x + 1)^2 (6 \cos x + 4 \cos 2x + 3) - \frac{i}{\sqrt{3}} (6 \sin x - \sin 2x - \sin 5x - \sin 6x + \sin 7x)$
	CSD($A_{U\bar{U}}, T_{U\bar{U}}$)
S_{acc12}	$-16\sqrt{\frac{2}{3}} \sin^4 \frac{x}{2} (17 \cos x + 16 \cos 2x + 14 \cos 3x + 8 \cos 4x + 3 \cos 5x + 8)$
S_{acc21}	$16\sqrt{\frac{2}{3}} \sin^4 \frac{x}{2} (16 \cos x + 17 \cos 2x + 13 \cos 3x + 8 \cos 4x + 3 \cos 5x + \cos 6x + 8)$
S_{acc13}	$64\sqrt{\frac{2}{3}} \sin^4 \frac{x}{2} \cos^2 \frac{x}{2} (\cos 2x + \cos 4x + 1)$
S_{acc31}	$-64\sqrt{\frac{2}{3}} \sin^4 \frac{x}{2} \cos^2 \frac{x}{2} (2 \cos x - \cos 2x + \cos 3x + \cos 5x)$
S_{acc23}	$16\sqrt{\frac{2}{3}} \sin^4 \frac{x}{2} (20 \cos x + 17 \cos 2x + 15 \cos 3x + 10 \cos 4x + 5 \cos 5x + \cos 6x + 10)$
S_{acc32}	$-16\sqrt{\frac{2}{3}} \sin^4 \frac{x}{2} (19 \cos x + 19 \cos 2x + 15 \cos 3x + 10 \cos 4x + 4 \cos 5x + \cos 6x + 10)$
S_{op12}	$-8\sqrt{\frac{2}{3}} \sin^4 \frac{x}{2} (4 \cos x + 3 \cos 2x + 3 \cos 3x + 2 \cos 4x + \cos 5x + 2) - \frac{i}{\sqrt{6}} (3 \sin x + 2 \sin 2x - 3 \sin 3x - 3 \sin 4x - \sin 5x + 2 \sin 6x + \sin 7x)$
S_{op21}	$-8\sqrt{\frac{2}{3}} \sin^4 \frac{x}{2} (4 \cos x + 3 \cos 2x + 3 \cos 3x + 2 \cos 4x + \cos 5x + 2) + \frac{i}{\sqrt{6}} (3 \sin x + 2 \sin 2x - 3 \sin 3x - 3 \sin 4x - \sin 5x + 2 \sin 6x + \sin 7x)$
S_{op13}	$32\sqrt{\frac{2}{3}} \sin^4 \frac{x}{2} \cos^2 \frac{x}{2} (\cos x + 2 \cos 2x + \cos 3x + \cos 4x + 1) - 16i\sqrt{\frac{2}{3}} \sin^3 \frac{x}{2} \cos^2 2x (2 \cos \frac{x}{2} + \cos \frac{3x}{2})$
S_{op31}	$32\sqrt{\frac{2}{3}} \sin^4 \frac{x}{2} \cos^2 \frac{x}{2} (\cos x + 2 \cos 2x + \cos 3x + \cos 4x + 1) + 16i\sqrt{\frac{2}{3}} \sin^3 \frac{x}{2} \cos^2 2x (2 \cos \frac{x}{2} + \cos \frac{3x}{2})$
S_{op23}	$-8\sqrt{\frac{2}{3}} \sin^4 \frac{x}{2} (2 \cos x + 1)^2 \cos 2x + \frac{i}{\sqrt{6}} (\sin 2x - 3 \sin 4x - 2 \sin 5x + \sin 6x + 2 \sin 7x)$
S_{op32}	$-8\sqrt{\frac{2}{3}} \sin^4 \frac{x}{2} (2 \cos x + 1)^2 \cos 2x - \frac{i}{\sqrt{6}} (\sin 2x - 3 \sin 4x - 2 \sin 5x + \sin 6x + 2 \sin 7x)$
	CSD($E_{U\bar{U}}, T_{U\bar{U}}$)
S_{acc12}	$-\frac{16}{3}\sqrt{2} \sin^4 \frac{x}{2} (2 \cos x + 1)^2 (3 \cos x + 3 \cos 3x + 2 \cos 4x + 2)$
S_{acc21}	$\frac{16}{3}\sqrt{2} \sin^4 \frac{x}{2} (22 \cos x + 21 \cos 2x + 17 \cos 3x + 12 \cos 4x + 5 \cos 5x + \cos 6x + 12)$
S_{acc13}	$-\frac{16}{3}\sqrt{2} \sin^4 \frac{x}{2} (2 \cos x + 1)^2 (3 \cos x + 6 \cos 2x + 3 \cos 3x + 2 \cos 4x + 2)$
S_{acc31}	$\frac{16}{3}\sqrt{2} \sin^4 \frac{x}{2} (37 \cos x + 33 \cos 2x + 29 \cos 3x + 18 \cos 4x + 8 \cos 5x + \cos 6x + 18)$
S_{acc23}	$-\frac{16}{3}\sqrt{2} \sin^4 \frac{x}{2} (14 \cos x + 15 \cos 2x + 13 \cos 3x + 6 \cos 4x + \cos 5x - \cos 6x + 6)$
S_{acc32}	$\frac{16}{3}\sqrt{2} \sin^4 \frac{x}{2} (13 \cos x + 15 \cos 2x + 11 \cos 3x + 6 \cos 4x + 2 \cos 5x + \cos 6x + 6)$
S_{op12}	$\frac{8}{3}\sqrt{2} \sin^4 \frac{x}{2} (8 \cos x + 9 \cos 2x + 7 \cos 3x + 4 \cos 4x + \cos 5x + 4) + \frac{i}{\sqrt{2}} (\sin x - \sin 3x + \sin 4x + \sin 5x - \sin 7x)$
S_{op21}	$\frac{8}{3}\sqrt{2} \sin^4 \frac{x}{2} (8 \cos x + 9 \cos 2x + 7 \cos 3x + 4 \cos 4x + \cos 5x + 4) - \frac{i}{\sqrt{2}} (\sin x - \sin 3x + \sin 4x + \sin 5x - \sin 7x)$
S_{op13}	$\frac{16}{3}\sqrt{2} \sin^4 \frac{x}{2} (2 \cos x + 1) \cos^2 2x + 4i\sqrt{2} \sin^3 x (\cos x + 2 \cos 2x + \cos 3x + \cos 4x + 1)$
S_{op31}	$\frac{16}{3}\sqrt{2} \sin^4 \frac{x}{2} (2 \cos x + 1) \cos^2 2x - 4i\sqrt{2} \sin^3 x (\cos x + 2 \cos 2x + \cos 3x + \cos 4x + 1)$
S_{op23}	$-\frac{8}{3}\sqrt{2} \sin^4 \frac{x}{2} (10 \cos x + 9 \cos 2x + 8 \cos 3x + 5 \cos 4x + 2 \cos 5x + 5) + 8i\sqrt{2} \sin^3 \frac{x}{2} \cos \frac{x}{2} (2 \cos x + 1)^2 \cos 2x$
S_{op32}	$-\frac{8}{3}\sqrt{2} \sin^4 \frac{x}{2} (10 \cos x + 9 \cos 2x + 8 \cos 3x + 5 \cos 4x + 2 \cos 5x + 5) - 8i\sqrt{2} \sin^3 \frac{x}{2} \cos \frac{x}{2} (2 \cos x + 1)^2 \cos 2x$